Nano Energy 73 (2020) 104736

Contents lists available at ScienceDirect

Nano Energy

journal homepage: http://www.elsevier.com/locate/nanoen

Multi-functional wind barrier based on triboelectric nanogenerator for power generation, self-powered wind speed sensing and highly efficient windshield

Yan Wang [a,b], Jianye Wang [a], Xiu Xiao [a], Siyuan Wang [a], Phan Trung Kien [a], Jiale Dong [a], Jianchun Mi [a,d], Xinxiang Pan [a,b], Hanfeng Wang [c,**], Minyi Xu [a,*]

[a] Marine Engineering College, Dalian Maritime University, Dalian, 116026, China
[b] School of Electronics and Information Technology, Guangdong Ocean University, Zhanjiang, 524088, China
[c] School of Civil Engineering, Central South University, Changsha, 410075, China
[d] College of Engineering, Peking University, Beijing, 100871, China

ARTICLE INFO

Keywords:
Triboelectric nanogenerator
Wind energy harvesting
Wind barrier

ABSTRACT

The integration of traditional wind barriers and novel wind energy harvesters is highly desirable for the conversion of wind energy to electricity while protecting transportations from strong wind. In this work, a multi-functional wind barrier integrated by manifold triboelectric nanogenerator (TENG) units is proposed and investigated. The TENG unit consists of two copper electrodes and one strip of fluorinated ethylene propylene (FEP) membrane whose two ends are fixed on a 3D printed channel. Based on the optimized structure of each TENG unit, a wind barrier is presently constructed by 66 TENG units connecting in parallel. It is found that the wind barrier can generate the output current and power of up to 440 μA and 26 mW at the wind speed of 10 m/s. It is also significant that the TENG-based wind barrier can harvest slipstream energy induced by passing vehicles. More importantly, the windshield efficiency of the TENG-based wind barrier is 35% higher than that of the traditional porous wind barrier, significantly improving the safety of transportations. In addition, each TENG unit of the wind barrier can work as a self-powered anemometer to monitor the condition of the wind barrier. Therefore, the present novel wind barrier has a great potential to apply for wind energy harvesting, self-powered wind speed sensing and highly efficient wind protection.

1. Introduction

To prevent derailment or overturning of high-speed trains and vehicles, wind barriers are usually installed on one or both sides of the line to create a relatively low local speed environment and improve the stability of high-speed vehicles under crosswinds [1–4]. Apparently, there is a huge amount of wind energy resources in the area where the wind barriers are installed. It is known that the conventional wind turbine is effective in harvesting wind energy but cannot act as a windshield due to its structural characteristics. In addition, the collision between turbines and wild animals which would lead to severe wildlife mortality and equipment maintenance still remains a thorny problem [5, 6]. Therefore, it is highly desired to design a novel wind barrier which can convert wind energy into electricity to power wireless sensor networks, as well as efficiently protect against strong wind.

Recently, triboelectric nanogenerator (TENG) has been developed to generate electrical output based on contact triboelectrification and electrostatic induction in response to an external mechanical stimuli [7–21]. A class of wind energy harvesters based on TENG have been introduced by converting flow-induced vibration into electricity [22–37, 56]. The first experimental study on a flutter-driven TENG was performed by Yang et al. [22] with a fluorinated ethylene-propylene (FEP) film between two aluminum foils. Results showed that the TENG could generate an output power of 0.16 mW under a loading resistance of 100 MΩ. To further enhance the electrical output, Wang et al. [23] connected 10 TENGs in parallel, and a maximum output power of 25 mW was generated under the loading resistance of 400 kΩ. The integration of manifold TENG units to increase energy output has become a developing

* Corresponding author.
** Corresponding author.
E-mail addresses: wanghf@csu.edu.cn (H. Wang), xuminyi@dlmu.edu.cn (M. Xu).

https://doi.org/10.1016/j.nanoen.2020.104736
Received 20 December 2019; Received in revised form 29 February 2020; Accepted 20 March 2020
Available online 2 April 2020

trend in practical applications but still needs to be studied systematically. Additionally, the TENG can serve as an active sensor of both wind speed and direction using its own electrical output without a secondary power source [38–40]. These reported flutter-driven TENGs have exhibited extraordinary advantages, including simple structure, low cost, robust, high efficiency and good expandability. Thus, TENG has a great potential to integrate with traditional wind barriers.

In the present work, a novel and multi-functional wind barrier constructed by manifold TENG units is proposed and systematically investigated. The TENG-based wind barrier has an excellent capability to harvest wind energy from natural wind and also the slipstream energy induced by passing vehicles. Note that the slipstream is often considered to be significantly harmful to surrounding people and structures, but it cannot be harvested by traditional methods due to its arbitrary direction and instability. More importantly, the windshield efficiency of the TENG-based wind barrier is found to be 35% higher than that of the traditional porous wind barrier, significantly improving the safety of transportations. In addition, the fluttering frequency of the FEP membrane in the TENG unit is found to be linear with the wind velocity, thus it can be used as an anemometer to monitor the condition of the wind barrier. Therefore, this work proves the advantages of the TENG-based wind barrier for wind-shielding, energy-harvesting, self-powered wind speed sensing, and provides a theoretical basis for its further extensive application.

2. Results and discussion

2.1. Structure and working principle of the TENG-based wind barrier

Fig. 1a illustrates the schematic diagram of the wind barrier that is composed of manifold TENG units. As shown in the insets of this figure, the TENG unit is made of two copper electrodes and one strip of FEP membrane fixed in a 3D printed polylactic acid (PLA) channel. A coordinate system is defined to better clarify the geometric structure of the TENG unit, as displayed in Fig. 1b. The origin of the coordinate system (x, y) is located at the center of the air gap. The TENG unit works in the freestanding contact mode with the dielectric membrane fluttering between the two electrodes. The sag (s) of the dielectric membrane is defined as the distance from the lowest point of the fully relaxed dielectric membrane to the origin of the coordinate. In addition, the width w, the air gap h_{ag} of the TENG unit, the thickness d_0 of the membrane and the charge density σ are also shown in Fig. 1a and b. All these parameters would affect the vibration of the membrane and the electrical performance of the TENG.

The detailed working mechanism is demonstrated in Fig. 1c. In the initial state, the dielectric membrane is in contact with the lower copper electrode under gravity effect. Due to the large electronegativity difference between the dielectric FEP material and copper, positive and negative triboelectric charges are generated on the surfaces of the copper electrode and the membrane respectively (Fig. 1ci). Under the action of wind disturbance, the membrane is separated from the lower copper electrode and vibrates upward. At this stage, triboelectric electrons flow from the upper copper electrode to the lower copper electrode through the external circuit, thereby generating a transient current flow (Fig. 1cii). When the membrane comes into contact with the upper copper electrode, all the positive charges are presented on this electrode (Fig. 1ciii). Subsequently, the reversed movement of the membrane leads to a reversed transfer of electrons through the external circuit (Fig. 1civ). Till now, a full cycle of electricity generation is completed and the mechanical energy of wind is converted into electricity successfully. Furthermore, the COMSOL Multiphysics software is employed to calculate the electrostatic field distribution of the TENG. The results are shown in Fig. S1 in the Supporting Information. Apparently, the simulation results are in consistent with the above analysis.

According to the theory of the contact-mode freestanding TENG, the governing equation for TENG can be written as [41]:

$$V = -\frac{1}{C}Q + V_{OC} = -\frac{d_0 + h_{ag}}{\varepsilon_0 S}Q + \frac{2\sigma\left(h_{ag}/2 - \omega\right)}{\varepsilon_0} \quad (1)$$

where V_{OC} is the open-circuit voltage and Q is the transferred charge. C, d_0, h_{ag}, ε_0 and S represent the capacitance of the TENG unit, the thickness of the membrane, the height of the air gap, the dielectric

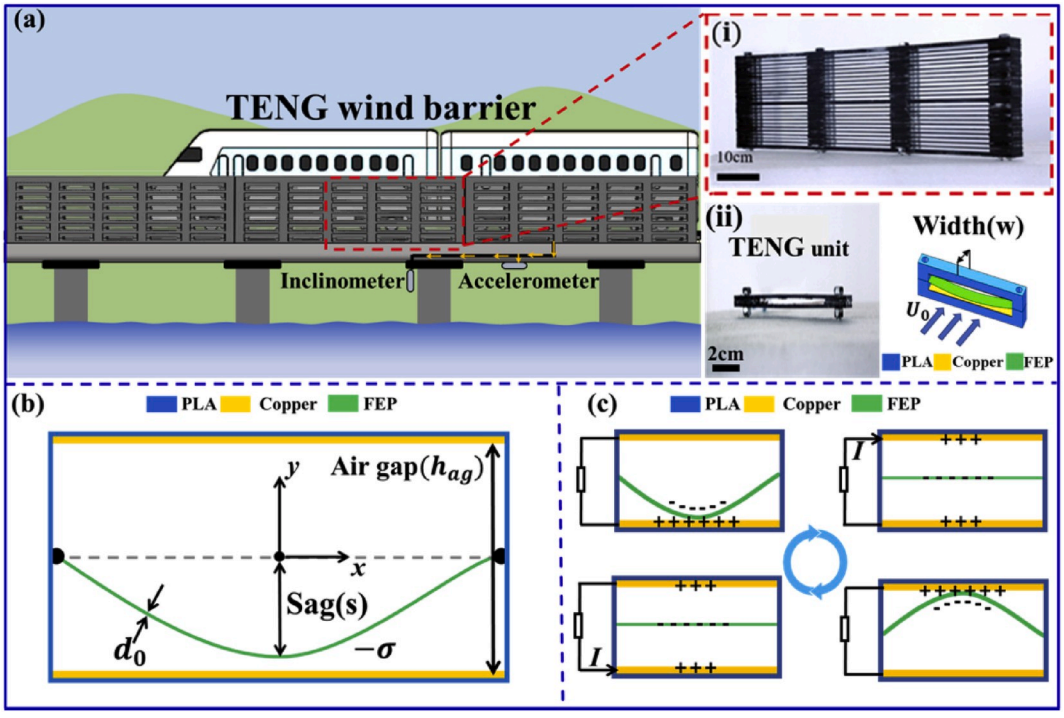

Fig. 1. Application scenario and working mechanism of the TENG-based wind barrier. (a) Application scenario of the TENG-based wind barrier, photograph of the TENG unit, and schematic diagram of the TENG unit. (b) Coordinate system of the TENG unit. (c) Working mechanism of the TENG unit.

constant in vacuum and the area size of the copper electrode layer, respectively. ω denotes the displacement of the dielectric membrane along y-coordinate due to elastic deformation and σ is the charge density. Flutter is a kind of vibration resulting from the coupling of aerodynamic forces and the elastic deformation of a structure [42,43]. When wind flows through the dielectric membrane, the membrane is subjected to aerodynamic force and starts to vibrate. The vibration of the membrane will further enhance the aerodynamic load, which in turn increases the vibration amplitude of the membrane. Theoretically, the motion of membrane can be derived from the Euler-Bernoulli beam theory [42], which is

$$m\frac{\partial^2\omega}{\partial t^2} - T_0\frac{\partial^2\omega}{\partial x^2} - \Delta p = 0 \tag{2}$$

where x represents the position of the dielectric membrane along x-coordinate, ω is the displacement of the dielectric membrane along y-coordinate due to elastic deformation, m is the mass of the membrane per unit length, T_0 is the axial internal force, and Δp is the pressure difference across the membrane.

During the vibration of the dielectric membrane, the membrane displacement ω experiences periodical variations under the action of transient pressure difference, leading to the generation of alternating current. It is worth noting that the sag (s) of the dielectric membrane, which is defined as the distance from the lowest point of the fully relaxed dielectric membrane to the origin of the coordinate [44], is always larger than half the height of the air gap. Therefore, the flutter of the dielectric membrane is confined by the channel. The dielectric membrane contacts with the upper/bottom copper electrodes when $|s| = h_{ag}/2$. With the further increase of ω, the dielectric membrane undergoes greater deformation and the effective contact area between the dielectric layer and the electrodes is enlarged. Furthermore, the contact area is also related to the width (w) of the membrane since it is in a rectangular shape. Therefore, we can conclude from the above analysis that the sag and width of the dielectric membrane as well as the height of the channel are the three main parameters that determine the fluttering characteristics of the membrane, as well as the electricity generation performance of the TENG unit.

2.2. Electrical output performance of the TENG-based wind barrier

Structural optimization experiments for the TENG unit are performed in an open-loop low-speed wind tunnel. The schematic of the experimental setup is shown in Fig. 2a. A TENG unit with an inner dimension of 100 × 10 × 3 mm^3 is first used in the wind tunnel experiment. It is known that the triboelectric performance of the dielectric material is one of the critical parameters that determines the electrical output of the TENG. Therefore, according to the triboelectric sequence of common materials, Poly tetra fluoroethylene (PTFE), benzene type polyimide (Kapton) and FEP are selected as the dielectric materials to test the power generation performance of the TENG unit. The results are shown in Fig. S2. Significantly, the application of FEP membrane can improve the electrical output of the TENG unit effectively. Therefore, the FEP membrane is adopted for the current work.

Thereafter, the three major parameters affecting the flutter characteristics of the FEP membrane as well as the electrical output of the TENG unit are studied and the results are displayed in Fig. 2b–e. The mean value and standard deviation of the critical wind speed are obtained by performing 5 times of the experiment. The test time and the number of samples in the structural optimization experiments are 30 s and 1000, respectively. Here, the data and the error bar in Fig. 2c–e are the mean value and the 'Mean ± Standard deviation' of the testing samples. The FEP membrane is expected to flutter once wind blows over membrane surface at a sufficiently high speed. As shown in Fig. 2b, the FEP membrane of $s/h_{ag} \leq 5/6$ do not flutter when the wind speed is below 3 m/s. This can be explained by the fact that the FEP membrane has its own stiffness to resist displacement when its two ends are fixed. To overcome the stiffness and to enable membrane flutter, the wind speed has to be sufficiently high. When s/h_{ag} is further enlarged, the critical wind speed rises sharply to 9.5 m/s. A greater s/h_{ag} indicates a severe state of curl and a larger mass of the FEP membrane. The increase in s/h_{ag} also results in a larger contact area between the membrane and the electrodes, thus increasing the amount of transferred charge. In fact,

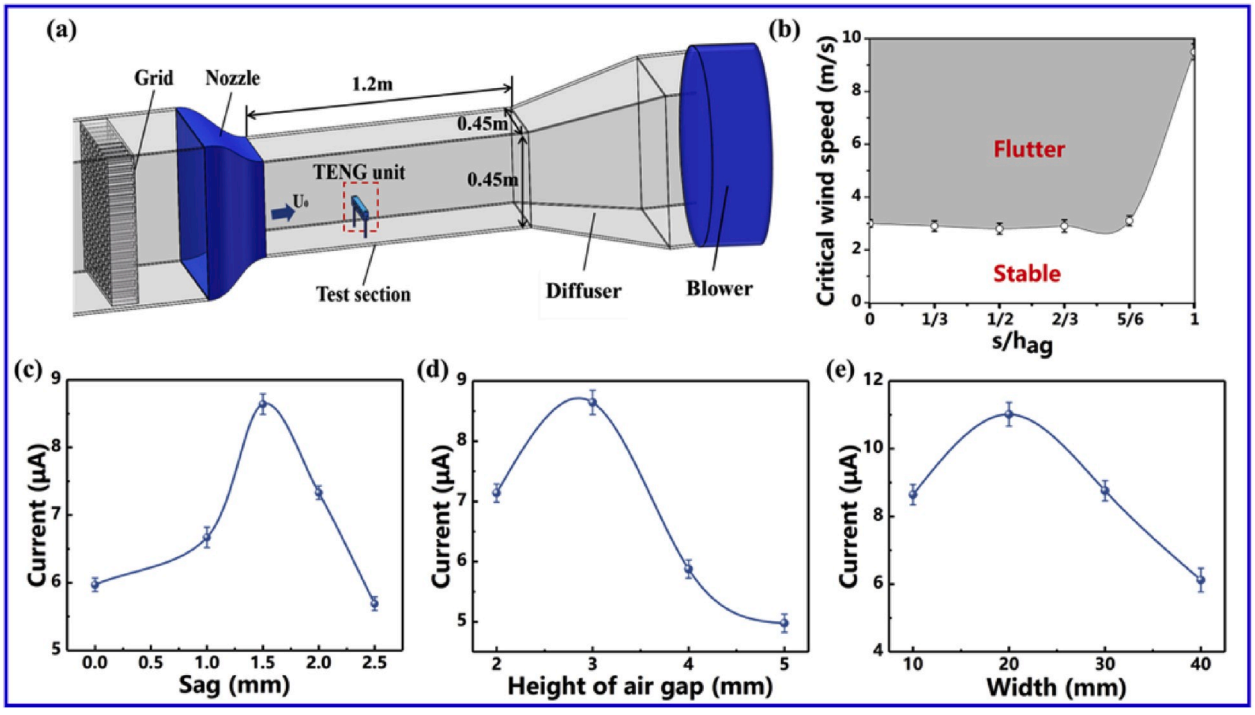

Fig. 2. Structural optimization experiments for the TENG unit in a wind tunnel. (a) Schematic of the experimental apparatus. (b) Critical wind speeds for the TENG units with different s/h_{ag}. Dependence of the output current on the (c) membrane sag, (d) air gap and (e) width of the membrane.

when the geometrical dimension of the TENG unit is fixed, there is an optimal s/h_{ag} that makes the TENG unit have the best electrical output performance. To find out the optimal fit between the sag and the height of air gap, a systematical experimental test with different $s/\ h_{ag}$ is conducted at the wind speed of 10 m/s. As shown in Fig. S3, the maximum current always presents at $s/h_{ag} = 1/2$ regardless of the height of the TENG unit. Therefore, by setting s/h_{ag} at the optimal value of 1/2, the structural optimization experiments for the TENG unit are conducted in subsequent. In addition, the width of the TENG unit also affects the critical wind speed of fluttering. Fig. S4 shows that the critical wind speed increases with the TENG width. As exhibited in Fig. 2c–e, when the TENG unit has an inner dimension of $100 \times 20 \times 3\ mm^3$, a maximum current of about 8.7 μA is achieved at the wind speed of 10 m/s. Correspondingly, a maximum output voltage of 114.1 V and a transfer charge of 37.2 nC are obtained, as shown in Fig. S5.

The output performance of the TENG unit is not only related to its geometric structure, but also to the specific wind condition. Fig. 3a-b demonstrates the dependence of the electrical output of the TENG unit on wind speed. When the wind speed is lower than 20 m/s, the output voltage of the TENG unit increases rapidly with the wind speed. More specifically, as the wind speed increases from 5 m/s to 20 m/s, the output voltage is increased from 32.7 V to 114.1 V. With the further increase of wind speed, the accumulation of polarized charge on the surface of the electrodes reaches a saturation state, and the open-circuit voltage achieves a maximum value of 114.1 V. However, the output current of the TENG unit continues to rise with the wind speed. At the wind speed of 30 m/s, the current can reach about 17.9 μA. Owing to the increase of wind speed, the fluttering frequency of the FEP membrane increases continuously. It is interesting to note that the frequency of the TENG electric signals is consistent with the flutter frequency of the membrane. A linear relationship between the wind speed and the flutter frequency is observed, as displayed in Fig. 3c. The flutter frequency of the membrane f can be expressed as $f = S_t U/L$ with U being the incoming mean wind speed, L being the length of the membrane, and S_t being the nondimensional parameter named Strouhal number. For the flapping flow, Shelley et al. [45] found that the Strouhal number which was based on the flag length was approximately 1.2. Dai et al. [46] used numerical simulations of pitching flexible plates and found a high efficiency regime around $S_t = 0.4$. These studies indicate that the value of S_t varies with the types of flows, but would be approximately constant for the same bluff body or membrane. Therefore, the flutter frequency of the membrane is proportional to the incoming mean wind speed. This suggests that TENG unit can be used to sense the wind speed by utilizing the linear relationship between the wind speed and the frequency of voltage signals.

Moreover, the flutter characteristics of the FEP membrane differs at different values of the turbulence intensity defined as $I = \frac{u_{RMS}}{\overline{U}}$, where u_{RMS} is the root-mean-square of the turbulent velocity fluctuations and $\overline{U}$ is the mean velocity. The response of the power generation performance of the TENG unit to wind turbulence intensity is investigated in the wind tunnel. The wind speed is set to 10 m/s, and the TENG output performances at three typical turbulence intensities, *i.e.* 0.5%, 5%, and 10% are tested by using different grids installed at the entrance of the test

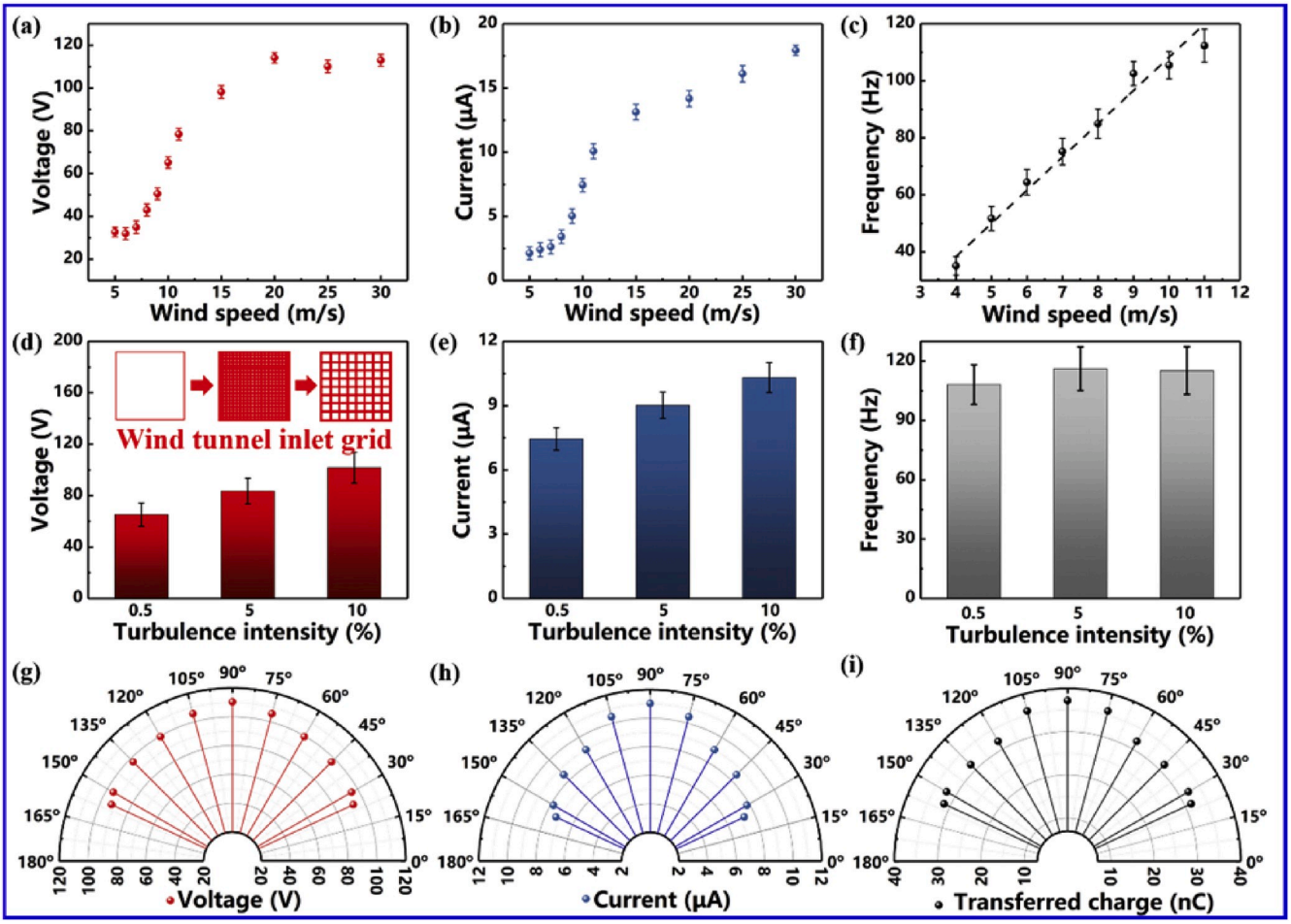

Fig. 3. Dependence of the power generation performance of the TENG unit on wind speed, turbulence intensity and wind direction. (a) Open-circuit voltage, (b) short-circuit current and (c) membrane flutter frequency versus the wind speed. (d) Open-circuit voltage, (e) short-circuit current and (f) membrane flutter frequency versus turbulence intensity. (g) Open-circuit voltage, (h) short-circuit current and (i) transferred charge of the TENG unit versus inlet wind direction.

section. The output voltage and current are measured respectively, and the results are displayed in Fig. 3d and e. Apparently, the increase in turbulence intensity can improve the electrical output of the TENG unit. As the turbulence intensity increases from 0.5% to 10%, the open-circuit voltage and short-circuit current are increased by 56.2% and 33.3%, respectively. However, the flutter frequency of the membrane seems to be independent of the turbulence intensity, as shown in Fig. 3f. The transferred charge Q of the TENG unit can be expressed as $Q = \sigma S$, with S being the contact area between the membrane and the electrodes, and σ being the charge density [47]. This suggests that a higher turbulence intensity may disturb the membrane vibration mode and increase local contact area S. Comparatively, the robust linear relationship between the incoming mean velocity and the flutter frequency indicates that the flutter frequency mainly depends on the mean velocity instead of turbulence intensity.

Researchers have found that a disorganized slipstream can be induced by high-speed vehicles [48,49]. Slipstream is often considered to be significantly harmful to surrounding people and structures. Due to its arbitrary direction and instability, it cannot be harvested by traditional methods. It is exciting to notice that the present TENG unit shows a superior electrical output performance over a wide wind direction. As exhibited in Fig. 3g–i, the TENG unit shows a best electrical output when the wind blows vertically. The output signal has some decrease when the wind direction deviates from the vertical direction. However, the open-circuit voltage, short-circuit current and transfer charge can still reach 93 V, 7.4 μA and 32 nC respectively when the wind direction is 65° from the vertical, indicating that the energy contained in the disorganized slipstream can be effectively harvested by the TENG unit. Therefore, the TENG-based wind barrier is able to harvest wind energy of slipstream by passing vehicles, and the TENG-based wind barrier can be used for harvesting slipstream energy in a breeze condition.

Upon understanding the output performance of the TENG unit, a power generation wind barrier integrated by 66 TENG units is designed to harvest wind energy. Fig. 4 shows the electrical output performance of the TENG-based wind barrier. As can be seen in Fig. 4a, the TENG unit can deliver a peak current of about 11 μA at the wind speed of 10 m/s. For the TENG-based wind barrier, the mean value of current peaks over the time interval of 6 s is 440 μA (Fig. 4b). As displayed in Fig. 4c, the peak current increases linearly from 40 μA to 440 μA when the number of TENG unit increases from 5 to 66. This indicates that, when the number of TENG units in the wind barrier is further increased, a larger electrical output is expected. In addition, under the matched loading resistance of 100 MΩ, the peak output power and the volume power density of single TENG unit with dimension of 100 × 20 × 3 mm^3 are 5.2 mW and 870 W/m^3 respectively (Fig. 4d). The peak output power can reach 26 mW under a loading resistance of 1 MΩ for the TENG-based wind barrier, as shown in Fig. 4e. As exhibited in Fig. 4f, the output power increases from 5.2 mW to 26 mW with the number of the TENG unit increasing. But it is interesting to note that the increase in power does not go linearly. In parallel circuits, the inverse of the total resistance is the sum of inversely each parallel resistance. Therefore, after manifold TENG units are connected in parallel, the total internal resistance becomes smaller than that in series.

The TENG-based wind barrier has been tested at the maximum wind speed of 30 m/s which is over Grade 12 on Beaufort scale for 10 min. It can produce about 820 μA at such wind speed, as shown in Fig. S6. But it is worthy to note that many membranes are broken under such severe wind condition. It is necessary to develop stronger material and further optimize the structure to deal with severe wind condition in the future. In addition, there are one rectified circuit and two wires connected to the top and bottom electrodes for each TENG unit. If the TENG-based wind barrier consists of hundreds and thousands of TENG units, the connection and layout of those wires would be a great challenge. Also, the rectified circuits would cause amount of energy consumption. Therefore, it is highly desired to propose a highly efficient energy management method.

2.3. Windshield effect of the TENG-based wind barrier

The fundamental function of the wind barrier is to protect the

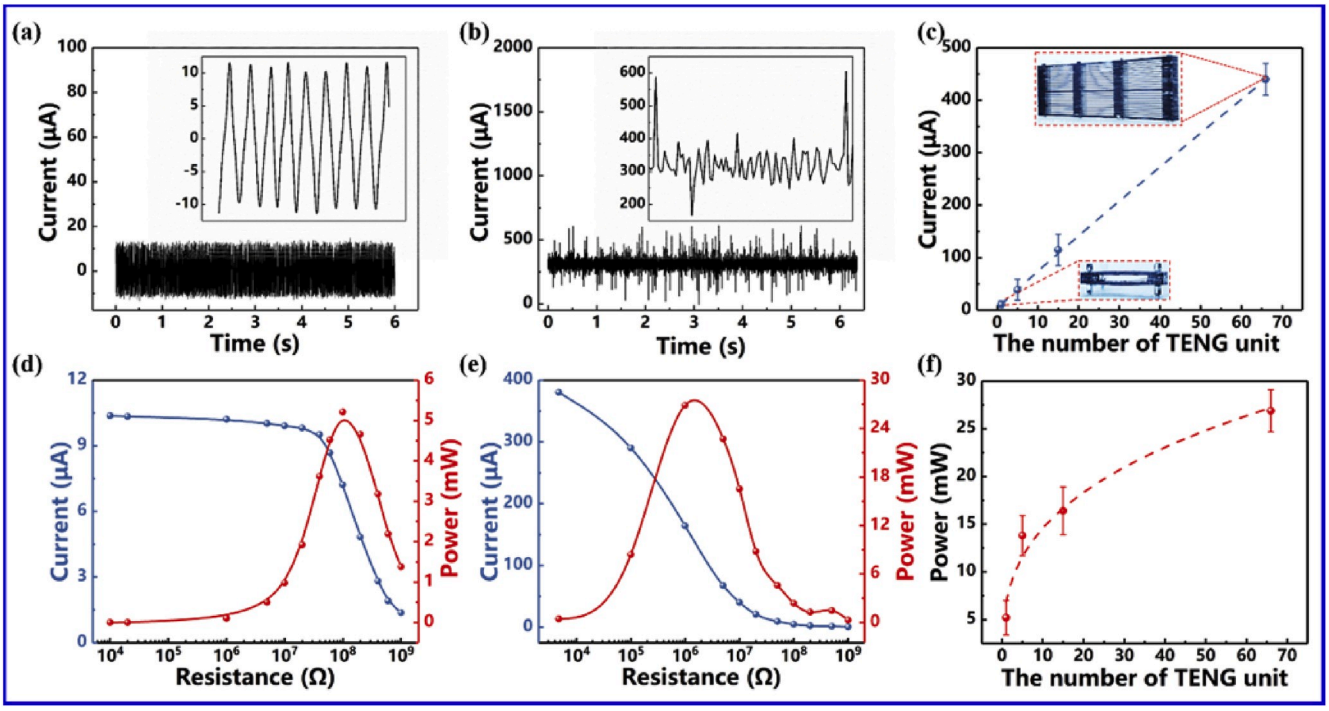

Fig. 4. The output performance of the TENG-based wind barrier. Typical output current of (a) the TENG unit and (b) the wind barrier integrated by 66 rectified TENG units. (c) Variation of the current with the number of TENG units. Dependence of the output current and power on the external resistance for (d) the TENG unit and (e) the TENG-based wind barrier. (f) The variation of the power with the number of TENG units.

transportations from wind load. Porosity is one of the most important parameters determining the windshield efficiency of the wind barrier [50]. The increase in porosity will result in a lower weight of the wind barrier, thereby reducing the load on the load-bearing structural components. However, if the porosity is too high, the lateral load of the barrier may exceed the wind load specified by the strength design, which will result in the aerodynamic instability of the barrier. The porosity of common wind barrier is 30%–50% [51]. Therefore, a wind barrier with the porosity of 45.4% is selected in this work. Smoke-wire visualization technique is utilized to analyze the flow field at the rear of the wind barrier and the results are shown in Fig. 5a and b. A fine high-resistance wire coated in oil stretched across the flow field. The diameter of the wire is 0.05 mm and its interference to the flow is assumed to be negligible. The wire can produce short bursts of smoke controlled electrically by resistive heating. The smoke follows the air currents, which allows the observer to visualize the flow. Most of the wind accelerates in the free space above the wind barrier and only a small amount of wind passes through the gaps of the wind barrier. Oncoming wind which is blocked by the wind barrier flows around the wind barrier and produces vortex shedding. Compared to the traditional wind barrier, the vortex shedding strength behind the TENG-based wind barrier is greatly enhanced. The reason is that once the FEP membrane starts flapping, it provides additional blocking effects for the flow. In other words, the actual porous ratio of the TENG wind barrier reduces when the FEP membrane flutters.

The velocity distribution behind the wind barrier is measured by a Cobra probe. By comparing Fig. 5c and d, it can be concluded that the wind speed at the rear of the TENG-based wind barrier is much smaller than that at the rear of the traditional wind barrier, especially in the area far from the wind barrier. This phenomenon suggests that the TENG-based wind barrier can produce a larger area with lower wind speed and form a larger recirculation zone. To further evaluate the windshield performance of the wind barrier, a coordinate system displaying in Fig. S7 is defined. The wake flow behind the wind barrier can be treated as a two-dimensional flow. Thus, the strength of the vortex shown in Fig. 5a and b can be estimated by the mean Z-axis vorticity $\omega_Z = \frac{1}{2}\left(\frac{\partial V}{\partial X} - \frac{\partial U}{\partial Y}\right)$ with U and V being the mean velocity in the X-axis and Y-axis direction. From the velocity distribution shown in Fig. 5c and d, the velocity gradient $\frac{\partial U}{\partial Y}$ at $X/H = 4$, $Y/H = 1$ is 0.6 s^{-1} and 0.2 s^{-1} for the TENG-based wind barrier and the traditional wind barrier, respectively. Thus, the vorticity ω_Z behind the TENG-based wind barrier would be greatly enhanced.

Furthermore, the wind reduction rate λ defined as follows is introduced [52],

$$\lambda = 1 - \frac{\frac{1}{X_2 - X_1}\int_{X_1}^{X_2} |U(Y = Y_0, Z = 0)| dX}{U_0} \quad (3)$$

where X_1 and X_2 are the initial and end positions of the measurement, Y_0 denotes the height that is selected to calculate the windshield efficiency and U_0 represents the oncoming wind speed. In the present experiment, $X_1/H = 0.2$, $X_2/H = 0.6$, $Y_0/H = 0.8$, $U_0 = 10$ m/s. According to the measurement results of the Cobra probe, the wind reduction rate of the traditional wind barrier is calculated to be 0.40. For the TENG-based wind barrier, the windshield efficiency is 0.54. Therefore, compared to the traditional wind barrier with the same porosity, the present TENG-based wind barrier can increase windshield efficiency by 35%.

Furthermore, many turbulent structures are formed when wind flows through the gaps of the wind barrier. It can be observed from Fig. 5e and f that, the flow structure behind the TENG-based wind barrier is severely disturbed due to the flutter of the FEP membrane, which results in a higher turbulence intensity. The result is in consistent with the result of Xu et al. [53]. The increase in turbulence intensity behind the wind barrier can greatly reduce the overturning torque of the vehicles. Meanwhile, in view of the turbulence intensity effects on the electrical output performance of the TENG unit, the increase in turbulence intensity can further increase the power generation of the TENG-based wind barrier and improve the wind shielding performance. Therefore, the as-fabricated TENG-based wind barrier exhibits a promising application on wind energy harvesting and wind shielding.

2.4. Demonstration of the TENG-based wind barrier

The demonstration experiments are conducted to illustrate the application of the TENG-based wind barrier. A number of lights are

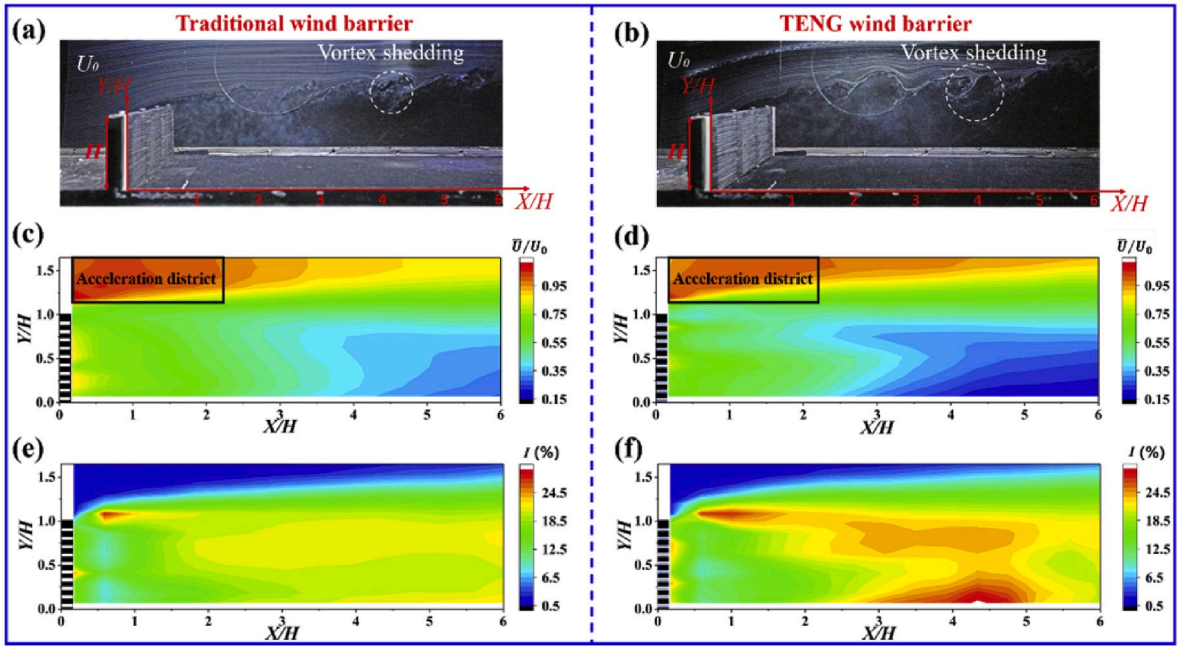

Fig. 5. Windshield performances of the TENG-based wind barrier and the traditional wind barrier. Smoke-wire flow visualizations of (a) the traditional wind barrier with a porosity of 45.4% and (b) the TENG-based wind barrier with a porosity of 45.4%; Velocity contours at the rear of (c) the traditional wind barrier and (d) the TENG-based wind barrier; Turbulence intensity contours at the rear of (e) the traditional wind barrier and (f) the TENG-based wind barrier.

arranged along the railway to remind people to be careful of the passing train or for illuminating. As can be seen in Fig. 6a and Supplementary Movie 1, the LED is directly lightened at the wind speed of 10 m/s. When the TENG-based wind barrier is used as a power source, each TENG unit is rectified in the circuit, as shown in Fig. S8. As presented in Fig. 6b and Supplementary Movie 2, the 'CAUTION'-shaped LEDs are powered by the TENG-based wind barrier. Meanwhile, a temperature and humidity sensor can be powered by 5 TENG units connected in parallel at the wind speed of 10 m/s, as shown in Fig. 6c and Supplementary Movie 3. Vertical direction wind speed can directly reflect the wind load of the wind barrier. As mentioned above, the frequency of the TENG unit output electric signal is consistent with the fluttering frequency of the membrane, and the TENG unit provides a feasible way to measure the wind speed in vertical direction. The wind speed U is obtained using the relationship between the frequency of current and wind speed, *i.e.* $U = 0.09f$. As shown in Fig. 6d and e and Supplementary Movie 4, the real-time wind speeds obtained by the TENG sensor and a commercial anemometer are compared and they agree well. Therefore, the TENG unit can be used as a self-powered anemometer. By measuring the wind speed, the condition of the TENG-based wind barrier is monitored.

Supplementary video related to this article can be found at https://doi.org/10.1016/j.nanoen.2020.104736

3. Conclusion

In summary, a multi-functional wind barrier integrated by multiple parallel connected TENG units is proposed in this work. The TENG unit consists of two copper electrodes and one strip of FEP membrane with its two ends fixed on a 3D printed PLA channel. The sag of the fully relaxed FEP membrane, the height of the air gap and the width of the membrane are the three major geometric factors determining the electrical output of the TENG unit. By conducting performance test experiments in a wind tunnel, a structure-optimized TENG unit with the dimension $100 \times 20 \times 3$ mm^3 is proposed. The power generation of the TENG unit increases with the wind speed (U) and turbulence intensity (I) when $U < 20$ m/s and $I < 15\%$. Significantly, the TENG unit shows a superior output performance as the wind direction varies from 25° to 155°. The TENG-based wind barrier is able to harvest wind energy of slipstream by passing vehicles. A maximum current of 11 μA and a peak output power of 5.9 mW are achieved under the matched loading resistance of 100 MΩ at the wind speed of 10 m/s. The power generation and windshield performances of the TENG-based wind barrier fabricated by a group of 66 TENG units connected in parallel are measured in a wind tunnel. The electrical output of the parallel-connected TENG device is linearly related to the number of TENG units. For the newly designed wind barrier, the peak output power can reach 26 mW under the loading resistance of 1 MΩ at the wind speed of 10 m/s, which can drive a household illuminating LED. Meanwhile, the TENG unit can be used as an anemometer to monitor the condition of the wind barrier. More importantly, compared to the traditional wind barrier with the same porosity, the TENG-based wind barrier can increase the windshield efficiency by 35%, which can greatly reduce the overturning torque of the vehicles and improve operation safety. Therefore, the as-fabricated TENG-based wind barrier has shown great potential applications in wind energy harvesting, highly efficient wind shielding and self-powered wind speed sensing.

4. Experimental section

4.1. Manufacture of the TENG-based wind barrier

The fabrication of the TENG unit is shown in Fig. S9. The PLA channel is printed by a 3D printer and its upper and lower surfaces are coated with copper electrodes. The FEP membrane has a thickness of 30 μm. The two ends of the membrane are fixed on the PLA channel. The membrane's sag can be adjusted by rotating the shaft at the end of the TENG unit. The TENG unit works in the freestanding contact mode. After the optimal structure of the TENG unit is determined, acrylic sheet with the dimension of $420 \times 20 \times 2$ mm is used as the substrate of the wind barrier for easy manufacturing. Four holes with a diameter of 8 mm are drilled on the acrylic sheet. The main structure of the wind barrier is fabricated by 23 acrylic sheets and some gaskets. 4 screws are inserted into the 23 acrylic sheets from top to bottom. The gap between the two acrylic sheets is divided into three parts with gaskets. The FEP membrane is set in the gap and the copper electrodes are pasted on the inner surface of the top and bottom substrates. The TENG-based wind barrier with 66 TENG units is completed as shown in Fig. S10 and its dimension is $420 \times 20 \times 112$ mm^3. When wind flows through the TENG-based wind barrier, the membrane can flutter periodically, thus producing alternating voltage and current signals.

4.2. Electrical output measurement

The structure optimization experiments for single TENG unit are

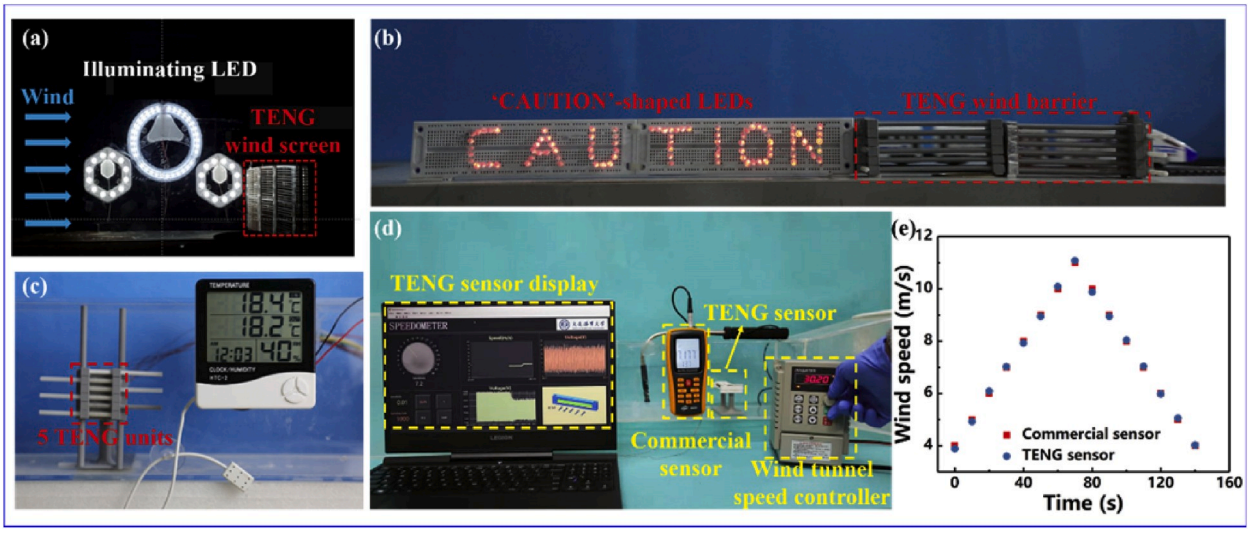

Fig. 6. Demonstrations of the TENG-based wind barrier as a power source and a sensor. The photograph of (a) household illuminating LED, (b) 'CAUTION'-shaped LED lights and (c) a temperature and humidity sensor by the TENG-based wind barrier. (d) The photograph of the real time wind speed measurement using the TENG sensor and a commercial sensor. (e) Comparison of TENG sensor and commercial wind speed sensor.

performed in a wind tunnel with a dimension of 0.45 m (width) × 0.45 m (height) × 1.2 m (length). The wind speed varies from 3 m/s to 42 m/s. As shown in Fig. S6, the size of the experimental domain is 6*H* (Length) × 3.75*H* (Width) × 3.75*H* (Height), where *H* is the height of the wind barrier. The blower is installed at the right end of the wind tunnel, as displayed in Fig. 2a. An inverter which can control the wind speed is used to control the rotating speed of the blower. Two screws are inserted into the two holes of the TENG unit, and the TENG unit is fixed by the nuts on the screws. Fig. S6 shows the definition of the coordinate system (*X, Y, Z*), with the origin *O* on the ground. The electrodes are connected to a Keithley 6514 electrometer to measure the open-circuit voltage, short-circuit current and transfer charge of the TENG. To understand the windshield performance of the wind barrier, Cobra probe is used to determine the flow field distribution behind the wind barrier. The measurements of the probe are carried out in the positions of $X/H =$ 0.17–6 downstream the wind barrier. Corresponding to the position with a certain X/H, 19 measuring points within the range of $Y/H =$ 0.07–1.65 are selected from top to bottom. The Cobra probe has a sampling frequency of 2000 Hz. The sampling duration at each measuring point is 30 s. The Cobra Probe is a multi-hole pressure probe, which is able to resolve 3-components of velocity and local static pressure in real time. A frequency response in excess of 2000 Hz means the Cobra Probe is especially suited to the measurement of turbulent flows. The reader may refer to Wang et al. [54] for more detail of the Cobra Probe.

Declaration of competing interest

The authors declare that they have no known competing financial interests or personal relationships that could have appeared to influence the work reported in this paper.

CRediT authorship contribution statement

Yan Wang: Conceptualization, Methodology, Writing - original draft. **Jianye Wang:** Formal analysis, Data curation. **Xiu Xiao:** Investigation, Writing - review & editing. **Siyuan Wang:** Visualization. **Phan Trung Kien:** Validation. **Jiale Dong:** Software. **Jianchun Mi:** Writing - review & editing. **Xinxiang Pan:** Funding acquisition. **Hanfeng Wang:** Supervision. **Minyi Xu:** Supervision, Writing - review & editing.

Acknowledgments

Y. Wang, J. Wang and X. Xiao contribute equally to this work. The authors are grateful for the joint support from the National Natural Science Foundation of China (Grant Nos. 51879022, 51979045, 51906029), the Fundamental Research Funds for the Central Universities, China (Grant No. 3132019330), and Projects for Dalian Youth Star of Science and Technology (Grant No. 2018RQ12).

Appendix A. Supplementary data

Supplementary data to this article can be found online at https://doi.org/10.1016/j.nanoen.2020.104736.

References

[1] C.J. Baker, J. Jones, F. Lopez-Calleja, J. Munday, J. Wind Eng. Ind. Aerod. 92 (2004) 547–563.
[2] S. Minoru, T. Katsuji, M. Tatsuo, J. Wind Eng. Ind. Aerod. 91 (2001) 209–218.
[3] S.A. Coleman, C.J. Baker, J. Wind Eng. Ind. Aerod. 36 (1990) 1383–1392.
[4] J. Zhang, G. Gao, T. Liu, Z. Li, J. Appl. Fluid Mech. 10 (2017) 1189–1200.
[5] J.W. Horn, E.B. Arnett, T.H. Kunz, J. Wildl. Manag. 72 (2008) 123–132.
[6] S.R. Loss, T. Will, P.P. Marra, Biol. Conserv. 168 (2013) 201–209.
[7] Z.L. Wang, L. Lin, J. Chen, S. Niu, Y. Zi, Triboelectric Nanogenerator, Springer, Berlin, Germany, 2016.
[8] Y. Chen, Y. Cheng, Y. Jie, X. Cao, N. Wang, Z.L. Wang, Energy Environ. Sci. 12 (2019) 2678–2684.
[9] J. Yang, X. Jia, J. Zou, Y. Chen, C. Xia, Adv. Energy Mater. 8 (2018) 1703133.
[10] B. Chen, Y. Yang, Z.L. Wang, Adv. Energy Mater. 8 (2018) 1702649.
[11] H. Phan, D.M. Shin, S.H. Jeon, T.Y. Kang, P. Han, G.H. Kim, H.K. Kim, K. Kim, Y. H. Hwang, S.W. Hong, Nano Energy 33 (2017) 476–484.
[12] S.B. Jeon, S. Kim, S.J. Park, M.L. Seol, D. Kim, K.C. Yong, Y.K.J.N.E. Choi, Nano Energy 28 (2016) 288–295.
[13] M. Taghavi, A. Sadeghi, B. Mazzolai, L. Beccai, V. Mattoli, Appl. Surf. Sci. 323 (2014) 82–87.
[14] Y. Jie, J. Ma, Y. Chen, X. Cao, N. Wang, Adv. Energy Mater. 8 (2017) 1802084.
[15] M. Ma, Z. Zhang, Q. Liao, G. Zhang, F. Gao, X. Zhao, Q. Zhang, X. Xun, Z. Zhang, Y. Zhang, Nano Energy 39 (2017) 524–531.
[16] X. Cao, M. Zhang, J. Huang, T. Jiang, J. Zou, N. Wang, Z.L. Wang, Adv. Mater. 30 (2018) 1704077.
[17] Y. Bian, T. Jiang, T. Xiao, W. Gong, X. Cao, Z. Wang, Z.L. Wang, Adv. Mater. Technol. 3 (2018) 1700317.
[18] X. Cao, Y. Jie, N. Wang, Z.L. Wang, Adv. Energy Mater. 6 (2016) 1600665.
[19] K. Zhao, Y. Yang, X. Liu, Z.L. Wang, Adv. Energy Mater. 7 (2017) 1700103.
[20] H. Zhao, X. Xiao, P. Xu, T. Zhao, L. Song, X. Pan, J. Mi, M. Xu, Z.L. Wang, Adv. Energy Mater. 9 (2019) 1902824.
[21] Y. Zou, P. Tan, B. Shi, H. Ouyang, D. Jiang, Z. Liu, H. Li, M. Yu, C. Wang, X. Qu, L. Zhao, Y. Fan, Z.L. Wang, Z. Li, Nat. Commun. 10 (2019) 2695.
[22] Y. Yang, G. Zhu, H. Zhang, J. Chen, X. Zhong, Z.-H. Lin, Y. Su, P. Bai, X. Wen, Z. L. Wang, ACS Nano 7 (2013) 9461–9468.
[23] S. Wang, X. Mu, X. Wang, A.Y. Gu, Z.L. Wang, Y. Yang, ACS Nano 9 (2015) 9554–9563.
[24] Z. Lin, B. Zhang, H. Guo, Z. Wu, H. Zou, J. Yang, Z.L. Wang, Nano Energy 64 (2019) 103908.
[25] P. Wang, L. Pan, J. Wang, M. Xu, G. Dai, H. Zou, K. Dong, Z.L. Wang, ACS Nano 12 (9) (2018) 9433–9440.
[26] W. Li, H. Guo, Y. Xi, C. Wang, M.S. Javed, X. Xia, C. Hu, RSC Adv. 7 (2017) 23208–23214.
[27] B. Dudem, D.H. Kim, J.S. Yu, Nano Res. (2017).
[28] Z. Zhao, X. Pu, C. Du, L. Li, C. Jiang, W. Hu, Z.L. Wang, ACS Nano 10 (2016) 1780–1787.
[29] Z. Quan, C.B. Han, T. Jiang, Z.L. Wang, Adv. Energy Mater. 6 (2016) 1501799.
[30] S. Nabavi, L. Zhang, Sensors 16 (2016) 1101.
[31] J. Bae, J. Lee, S. Kim, J. Ha, B.S. Lee, Y. Park, C. Choong, J.B. Kim, Z.L. Wang, H.-Y. Kim, J.J. Park, U.I. Chung, Nat. Commun. 5 (2014) 4929.
[32] S. Wang, X. Wang, Z.L. Wang, Y. Yang, ACS Nano 10 (2016) 5696–5700.
[33] Y. Xi, H. Guo, Y. Zi, X. Li, J. Wang, J. Deng, S. Li, C. Hu, X. Cao, Z.L. Wang, Adv. Energy Mater. 7 (2017) 1602397.
[34] H. Guo, X. He, J. Zhong, Q. Zhong, Q. Leng, C. Hu, J. Chen, L. Tian, Y. Xi, J. Zhou, J. Mater. Chem. A 2 (2014) 2079–2087.
[35] X. Wang, Y. Yang, Nano Energy 32 (2017) 36–41.
[36] X. Liu, K. Zhao, Y. Yang, Nano Energy 53 (2018) 622–629.
[37] L. Zhao, H. Li, J. Meng, A.C. Wang, P. Tan, Y. Zou, Z. Yuan, J. Lu, C. Pan, Y. Fan, Y. Zhang, Y. Zhang, Z.L. Wang, Z. Li, Adv. Funct. Mater. (2019) 1907999.
[38] M. Xu, Y.C. Wang, S.L. Zhang, W. Ding, J. Cheng, X. He, P. Zhang, Z. Wang, X. Pan, Z.L. Wang, Extrem. Mech. Lett. 15 (2017) 122–129.
[39] H. Guo, X. Pu, J. Chen, Y. Meng, M.H. Yeh, G. Liu, Q. Tang, B. Chen, D. Liu, S. Qi, C. Wu, C. Hu, J. Wang, Z.L. Wang, Sci. Robot. 3 (20) (2018) eaat2516.
[40] D. Kim, I.-W. Tcho, Y.-K. Choi, Nano Energy 52 (2018) 256–263.
[41] S. Niu, Y. Liu, S. Wang, L. Lin, Y.S. Zhou, Y. Hu, Z.L. Wang, Adv. Mater. 25 (2013) 6184–6193.
[42] S. Tiomkin, D.E. Raveh, J. Fluid Struct. 71 (2017) 143–163.
[43] D. Zhao, S. Li, Y. Zhang, J. Liu, Math. Probl Eng. 2018 (2018) 1–11.
[44] H. Minami, Y. Okuda, S. Kawamura, Experimental Studies on the Flutter Behaviour of Membranes in a Wind Tunnel, Thomas Telford Publishing, London, 1993.
[45] M. Shelley, N. Vandenberghe, J. Zhang, Phys. Rev. Lett. 94 (2005), 094302.
[46] H. Dai, H. Luo, P.J.S.A.F. Sousa, J.F. Doyle, Phys. Fluids 24 (2012) 101903.
[47] Z.L. Wang, L. Lin, J. Chen, S. Niu, Y. Zi, Triboelectric Nanogenerators, Springer, Berlin, Germany, 2016.
[48] C. Xia, H. Wang, X. Shan, Z. Yang, Q. Li, J. Wind Eng. Ind. Aerod. 168 (2017) 177–189.
[49] C. Xia, H. Wang, D. Bao, Z. Yang, Exp. Therm. Fluid Sci. 98 (2018) 381–396.
[50] S.J. Lee, H.C. Lim, Fluid Dynam. Res. 28 (2001) 209–221.
[51] L. Procino, H. Kozmar, G. Bartoli, A. Borsani, 6th International Colloquium on: Bluff Body Aerodynamics & Applications, Milano, 2008.
[52] J.D. Wilson, T.K. Flesch, Bound-Layer Meteorol. 109 (2003) 191–224.
[53] M. Xu, M. Wu, J. Mi, Exp. Therm. Fluid Sci. 106 (2019) 226–233.
[54] H. Wang, Z. Yu, Z. Chao, X. He, J. Wind Eng. Ind. Aerod. 148 (2016) 34–44.
[56] Q. Zeng, Y. Wu, Q. Tang, W. Liu, J. Wu, Y. Zhang, G. Yin, H. Yang, S. Yuan, D. Tan, C. Hu, X. Wang, Nano Energy (2020), 104524.